



Effect of Triangular Lip Wall on the Performance of a Stationary Oscillating Water Column Device at Various Wave Conditions Using Reynolds-averaged Navier-Stokes (RANS) Model

R. Ranjan Manjul and P. Deb Roy [†]

Department of Mechanical Engineering, NIT, Silchar, Assam - 788 010, India

[†]Corresponding Author Email: pdebroy@mech.nits.ac.in

ABSTRACT

One of the most inexhaustible forms of energy is the ocean wave. The conversion of this energy into a useful form of electrical energy is possible by a device of oscillating water column (OWC). This work aims to numerically analyse the effect of the triangular lip wall of the OWC wave energy converter on the hydrodynamic efficiency at different wave steepness conditions (H_i/λ), orifice ratios (ε), and relative openings (σ). This analysis uses commercial computational fluid dynamics (CFD) code ANSYS FLUENT software in a 3D numerical wave tank. The governing equations are discretized using FVM formulation, and the $k-\varepsilon$ turbulence model is used. The inlet velocity method is used to generate the waves. The model was validated and verified with the experimental model published by Çelik and Altunkaynak (2019) and implemented for further improvement. The hydrodynamic efficiency (E_{ff}) of the new model increases with relative openings increases and also increases with the decreases in wave steepness. This study shows an optimum efficiency of 76.30% at $\varepsilon_4 = 1.03\%$, $\sigma = 75\%$, and $H_i/\lambda = 0.02$. The information obtained from this numerical investigation of a new model is a highly relevant source, and it provides foresight in the design of the OWC wave energy converter.

Article History

Received November 28, 2024
Revised March 15, 2025
Accepted April 9, 2025
Available online June 3, 2025

Keywords:

Oscillating water column 45°
Triangular lip wall
Hydrodynamic efficiency
Relative opening
Orifice ratio
Reynolds-averaged Navier-Stokes (RANS)- volume of fluid (VOF)
Computational fluid dynamics

1. INTRODUCTION

The growing energy consumption and its adverse effect on climate change have led to an increased focus on developing clean and renewable energy sources. Of all renewable energy sources, ocean energy stands out as one of the most easily available energy throughout the globe (Pontes & Falcão, 2001; Pinson et al., 2012). Key technologies of the ocean wave include OWC, Wave Dragon, Tidal WEC, Pelamis WEC, etc. The oscillating water column (OWC) is a device that extracts PTO from sea waves. Falcão and Henriques (2016) studied and reviewed the mechanism of oscillating water columns (OWC) wave energy converter (WEC) in detail. Different scientists proposed fixed and floating types of technology. Whittaker et al. (1993) developed land-fixed OWC, and Washio et al. (2000) and Hotta et al. (1988) developed floating OWC.

The present study is on the triangular lip wall OWC model to understand the performance of OWC under different wave steepness conditions. The device is a vertical water column type; the upper section is air, and the lower section is seawater. The water in the chamber

oscillates due to the incident wave, and the air becomes compressed and expands (Fig. 1).

Several researchers have been trying to improve the design of the OWC device to develop its performance analytically or experimentally. The authors Malmo and Reitan (1985, 1986) worked on the lip wall design of the OWC device in their research. Bouali and Larbi 2013, numerically investigated the efficiency of an OWC by changing the different orientations of the lip wall. They observed that the orientation of the front wall in counter flow direction at a 180° angle is the best configuration. Çelik and Altunkaynak (2018) physically investigated the performance of the OWC system at various underwater front wall openings. Çelik and Altunkaynak (2020) experimentally investigated and verified numerically the free decay tests of an OWC at various underwater front wall openings of the chamber and orifice sizes. Çelik and Altunkaynak (2021) experimentally investigated water velocity in the column and air pressure. They observed a relation between wave pressure and height with the wave frequency. Further, Celik (2022), experimentally found the outcome of front wall geometry on the performance of

NOMENCLATURE			
A_o	cross-sectional area of the orifice	\bar{u}_i	average velocity
A_w	free surface area inside the owc chamber	$v(t)$	free surface velocity inside the chamber
a_i	wave amplitude	\bar{V}	velocity vector
b	length of the owc device	w	width of the owc device
$C_{\mu}, C_{\varepsilon 1}, C_{\varepsilon 2}$	empirical coefficients	$\Delta x, \Delta y, \Delta z$	size of elements
c	orifice diameter	β	lip wall angle
E_{ff}	hydrodynamic efficiency	δ	opening height of the chamber
E_{input}	incident wave power	λ	wave length
E_{output}	output power	ε	orifice ratio
F_h	flume height	ε	turbulence dissipation rate
F_l	flume length	μ	dynamic viscosity
F_{wgz}	wave generating zone	μ_t	eddy viscosity
F_{dz}	damping zone	μ_w	viscosity of water
G_k	turbulent energy production	μ_a	viscosity of air
g	acceleration due to gravity	ω_i	angular frequency
H_i	wave height	ρ	air-water mixture density
h	water depth	ρ_a	air density
k	turbulence kinetic energy	ρ_w	water density
k_i	wave number	σ	relative opening
$p(t)_{air}$	fluctuating air pressure	$\sigma_k, \sigma_\varepsilon$	empirical coefficients
\bar{P}	average pressure	τ_{ij}	viscous shear stress of the mean flow
T	time period	τ'_{ij}	reynold's stress due to velocity fluctuations

the OWC at various applied PTO damping levels. He observed underlip geometry with a circular cross-section, providing the maximum performance for all conditions. Open-source and commercial software CFD are becoming more attractive to researchers as powerful technology. Using Ansys Fluent software, [Marjani et al. \(2008\)](#) examined the hydrodynamic efficiency of the OWC. [López et al. \(2014\)](#) conducted a study using the Reynolds-averaged Navier-Stokes (RANS) equations to assess the damping impact of oscillating water column (OWC) devices. [Iturrioz et al. \(2015\)](#) used the Open FOAM software to assess the effectiveness of 3D modeling in the context of the Oscillating Water Column (OWC) model. [Simonetti et al. \(2017\)](#) verified the correctness of the efficiency and validated it. Recently, [Rodríguez et al. \(2023\)](#) used CFD code Ansys Fluent software to investigate the hydrodynamic performance of OWC devices at random wave circumstances. They found a positive correlation between wave height and pressure at specific points outside, inside, and toward the tip of the front wall. [Ranjan and DebRoy \(2023a\)](#) researched the hydrodynamic performance by numerical simulation of land fixed bottom parabolic OWC using Ansys Fluent software and validated it with experimental data. Also, [Ranjan and DebRoy \(2023b\)](#) numerically investigated the efficiency of OWC devices at various wave conditions.

Various researchers experimentally determine the performance of the OWC device in the laboratory. [Thiruvankatasamy and Neelamani \(1997\)](#) observed that the efficiency and wave steepness of OWC devices are inversely related. [Tseng et al. \(2000\)](#) found that the lip wall influences hydrodynamic efficiency in their 1/20 scale model ([Morris-Thomas et al., 2007](#)). [Gouaud et al. \(2010\)](#), experimental results match the numerical results. Liu examined the efficiency of an OWC device in 2008

and also by [Dizadji and Sajadian in 2011](#). Various bottom shapes of the OWC device play an essential role in exploring efficiency that was done experimentally ([Ashlin et al. 2016](#)). The opening ratio of the OWC device significantly influences efficiency, and the numerical results match the experimental results ([Ning et al., 2015](#)). [Ning et al. \(2016\)](#) investigated the physical model of the OWC device. [Liu et al. \(2016\)](#) conducted an experimental study on the PTO impulse turbine's, which influence on OWC performance. They optimized the orifice shape due to pressure drops in the turbine. Further, [Yadav and Deb Roy \(2022\)](#) studied shallow water stable linear wave theory using the CFD technique.

A deep review of the previous literature shows that the researchers mainly examined floating and fixed-type OWC WEC under various wave conditions to determine the PTO damping. The former researchers studied the different geometrical shapes of the OWC model that influence the efficiency of the OWC device. Various opening heights of the chamber, different bottom profiles, and the shape of the orifice are the different geometrical shapes. They use different numerical techniques such as computational Fluid Dynamics (CFD), Boundary Element Method (BEM), and experimental methods to solve the problems. However, careful attention is required to the hydrodynamic efficiency of the OWC devices as the water is reflected from the front wall of the OWC. Relative depth, wave steepness, relative opening, and orifice ratio are all required in detailed studies. Previous researchers did not carefully concentrate on the effect of the front wall shape, which plays an essential role in the performance of OWC devices. The air passing out during exhalation from the chamber and entering during inhalation into the chamber is a critical study of streamline motion, which researchers do not focus on deeply. Moreover, researchers

insufficiently focus on the oscillating motion of water within the chamber. Damage to the OWC front wall due to variations in water surface elevation inside and outside the chamber requires further study.

Vicinanza et al. (2014) reviewed innovative rubble mound breakwaters for overtopping wave energy conversion. Vicinanza et al. (2019) also reviewed innovative harbor breakwaters for wave-energy conversion. Simonetti and Cappietti (2021) reduce the harbour agitation by modifying the OWC structure. Carlo et al. (2023) numerically and experimentally studied U-OWC wave energy converter hydrodynamic performance. Cruz-Pérez et al. (2024) investigate and evaluate a SWOT Analysis of the Benefits of Hydropower Energy in Four Archipelagos. Rusvan et al. (2024) experimentally investigated Tidal Energy Potential Using a Two-Way Tidal Energy Model with a 1:100 scale prototype model in the laboratory with several predetermined variations. Sukkee and Kongphan (2024) numerically studied to enhance the production of metal powder production using CFD with Convergent-Divergent Nozzles in Wire Arc Atomization. Teixeira et al. (2013) numerical study of the aerodynamic and hydrodynamic flows and performance of an onshore OWC energy extraction device, using a code based on Navier-Stokes equations. Brito et al. (2020) explored the flow dynamics on the front face of an oscillating wave surge converter through experimental investigations. Gonçalves et al. (2020) numerically investigate the influence of air compressibility effects on an oscillating water column.

The key objective and innovation of this work was to analyze the influence of the triangular lip wall of the OWC wave energy converter on hydrodynamic performance by considering variations in wave conditions, orifice ratios, and relative openings. The study carefully examines pneumatic air pressure distribution over time, water surface motion, streamlined flow, and vortex formation near the triangular lip wall of the OWC device. The model is validated with the results of Çelik and Altunkaynak (2019), and it shows good agreement.

The overall organization of this paper is as follows: section 1 reviews the previous report and finds the research gap and objective. Section 2 discusses the governing equations (GE) using ANSYS FLUENT software. Section 3 describes the geometry of the OWC. In sections 3.3 and 3.4, convergence tests and model validation are discussed. Finally, the results and conclusions of the present study are summarised in Sections 4 and 5.

2. MATHEMATICAL FORMULATION

2.1 Governing Equation

Governing equations are continuity and RANS equations used to solve the incompressible turbulence fluid.

$$\frac{\partial \bar{u}_i}{\partial x_i} = 0 \quad (i = 1, 2, 3) \quad (1)$$

$$\rho \left[\frac{\partial \bar{u}_i}{\partial t} + \bar{u}_j \frac{\partial \bar{u}_i}{\partial x_j} \right] = - \frac{\partial \bar{p}}{\partial x_i} + \left(\frac{\partial \tau_{ij}}{\partial x_j} + \frac{\partial \tau'_{ij}}{\partial x_j} \right) + \rho g_i \quad (2)$$

where τ_{ij} is the viscous shear stress of the mean flow, and τ'_{ij} is Reynold's stress due to velocity fluctuations. \bar{u}_i , \bar{p} and ρ are the average velocity, pressure, and density. g is the acceleration of gravity. $\mu_e = \mu + \mu_t$, μ ($= 1.002 \times 10^{-6}$ m²/s) is the fluid viscosity and μ_t turbulent eddy viscosity. The indices $i, j = 1, 2, 3$ refer to the three-dimensional velocity components (u, v, w) or (u_1, u_2, u_3) and the spatial coordinates (x, y, z) or (x_1, x_2, x_3). The k- ϵ turbulence model (Lauder, 1989) is adopted for this analysis. The differential transport equations, turbulent kinetic energy k , and the turbulent dissipation rate ϵ are expressed as follows.

$$\tau_{ij} = \mu_e \left(\frac{\partial u_i}{\partial x_j} + \frac{\partial u_j}{\partial x_i} \right) \quad (3)$$

$$\tau'_{ij} = -\rho \overline{u'_i u'_j} \quad (4)$$

$$k = \frac{1}{2} \overline{u'_i u'_i} \quad (5)$$

$$\epsilon = \mu \frac{\partial u'_i}{\partial x_j} \frac{\partial u'_i}{\partial x_j} \quad (6)$$

$$\frac{\partial}{\partial t} (\rho k) + \frac{\partial}{\partial x_i} (\rho k \bar{u}_i) = \frac{\partial}{\partial x_j} \left[\left(\mu + \frac{\mu_t}{\sigma_k} \right) \frac{\partial k}{\partial x_j} \right] + \rho G_k - \rho \epsilon \quad (7)$$

$$\frac{\partial (\rho \epsilon)}{\partial t} + \frac{\partial}{\partial x_i} (\rho \epsilon \bar{u}_i) = \frac{\partial}{\partial x_j} \left[\left(\mu + \frac{\mu_t}{\sigma_\epsilon} \right) \frac{\partial \epsilon}{\partial x_j} \right] + \frac{\epsilon}{k} (c_{\epsilon 1} G_k - c_{\epsilon 2} \rho \epsilon) \quad (8)$$

$$\mu_t = \frac{c_\mu \rho k^2}{\epsilon} \quad (9)$$

$$G_k = \frac{\mu_t}{\rho} \left(\frac{\partial \bar{u}_i}{\partial x_j} + \frac{\partial \bar{u}_j}{\partial x_i} \right) \frac{\partial \bar{u}_i}{\partial x_j} \quad (10)$$

where σ_k and σ_ϵ are the turbulent Schmidt numbers, G_k = Production term, and the values of constants for the above equations are as follows: $C_{\epsilon 1} = 1.44$; $C_\mu = 0.09$; $C_{\epsilon 2} = 1.92$; $\sigma_\epsilon = 1.3$; $\sigma_k = 1$.

The volume of fluid (VOF) method is adopted to capture the interface of the two immiscible fluids at the free surface simultaneously (Hirt and Nichols, 1981). From a cell-volume averaged perspective, $f_i = 0$ means the cell contains air, $f_i = 1$ means the cell contains water, and the cell includes an interface between the air and water volume, representing $0 < f_i < 1$. Therefore, the equation for the volume fraction is:

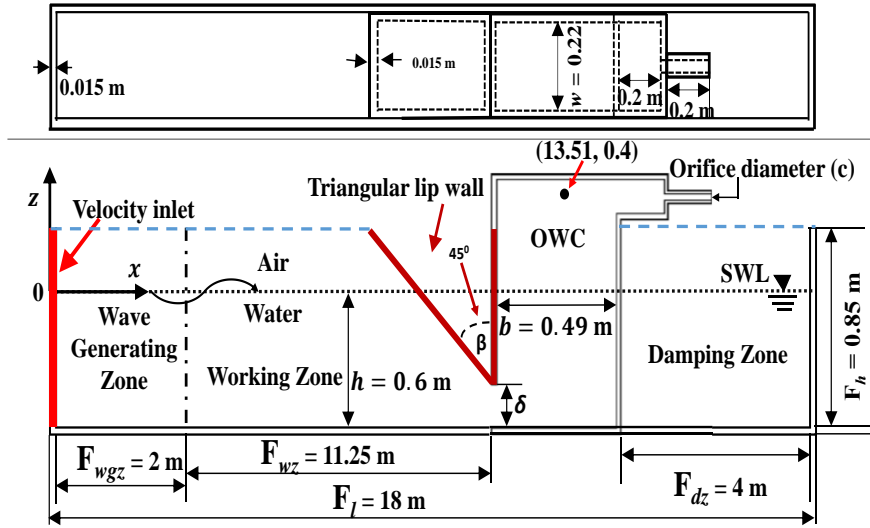


Fig. 1 Numerical wave tank and triangular lip wall OWC mechanism

$$\frac{\partial f_i}{\partial t} + \nabla \cdot (f_i \bar{V}) = 0 \quad (11)$$

$$\sum_{i=1}^2 f_i = 1 \quad (12)$$

Here \bar{V} is the velocity vector. Eqs (13) & (14) are the density and viscosity of the air-water mixture.

$$\rho = f_i \rho_w + (1 - f_i) \rho_a \quad (13)$$

$$\mu = f_i \mu_w + (1 - f_i) \mu_a \quad (14)$$

Where ρ_w = density of water, ρ_a = density of air, μ_w = water viscosity, and μ_a = air viscosity.

2.2. OWC Hydrodynamic Efficiency

Hydrodynamic efficiency is the ratio of pneumatic output power to the power of the corresponding incident wave. The efficiency at the orifice is utilized to generate electrical power through the prime mover. The average pneumatic output power (E_{output}) represents the energy absorbed by the OWC from waves over a wave period T . It is determined as the time-averaged product of the flow rate $A_w v(t)$ and the air pressure variation $p(t)_{air}$ within the chamber. Here, A_w is the free surface area inside the OWC chamber, and $v(t)$ is the free surface water velocity inside the chamber. Therefore, the pneumatic output power (E_{output}) is generated in the orifice, and the incident wave power (E_{input}) is per unit width (Boualia and Larbib, 2013), as shown in the following equations

$$E_{output} = \frac{1}{T} \int_t^{t+T} p(t)_{air} A_w v(t) dt \quad (15)$$

$$E_{input} = \frac{1}{2} \rho g a_i^2 \frac{\omega_i}{k_i} \left\{ \frac{1}{2} \left(1 + \frac{2k_i h}{\sinh(2k_i h)} \right) \right\} \left\{ 1 + \frac{9a_i^2}{16k_i^4 h^6} \right\} \quad (16)$$

where a_i , ω_i , and k_i are the amplitude, angular frequency, and the wave number of the incident wave, respectively, and h is the water depth. The frequency and wave number are given below:

$$\omega_i = \frac{2\pi}{T} \quad (17)$$

$$k_i = \frac{2\pi}{\lambda} \quad (18)$$

where T is the incident wave period.

The performance of an OWC is the hydrodynamic efficiency (E_{ff}) in the present problem is determined by the ratio of pneumatic output power (E_{output}) and the corresponding incident wave power ($E_{input} \times w$).

$$E_{ff} = \frac{E_{output}}{E_{input} \times w} \quad (19)$$

Where w is the width of the OWC.

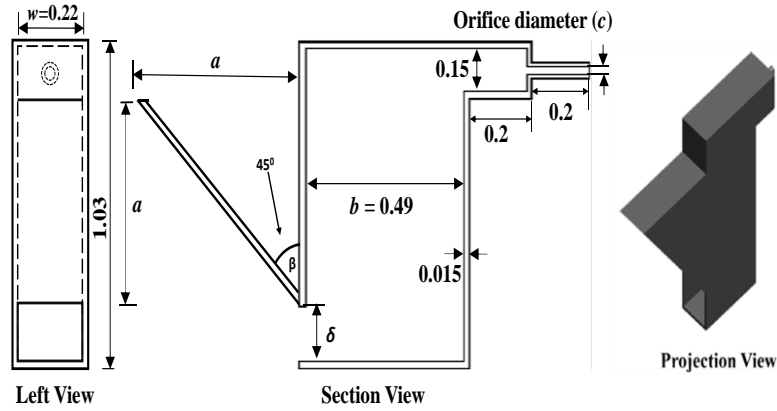
3. NUMERICAL MODEL

3.1. Tank Geometry

Figure 1 shows the computational domain of the OWC devices and the Numerical Wave Tank (NWT). The inlet velocity method developed Second-Order Stokes waves within a numerical wave tank. The waves travel in a propagation direction. The upper portion of the wave tank is in direct contact with the atmosphere. The no-slip boundaries are the right and bottom walls of the wave tank. The coordinate system in Cartesian coordinates is Oxz . The x -axis represents the direction of propagation, while the vertical axis is the z -axis. The y -axis is orthogonal to the Oxz plane. Figure 1 shows the following variables: tank height F_h (=0.85m), wave generating zone F_{wgz} (=2m), tank length F_l (=18m), damping zone F_{dz} (=4m), water depth h (=0.6m), lip wall angle β (=45 $^\circ$) and OWC opening = δ .

3.2. Geometry of the OWC

Figure 2 displays the geometry of the OWC model used in the present investigation and also shows the 3D CAD design of the OWC device. The observation point (13.51,0.4) is at the center of the OWC chamber. Two



All Dimensions are in m.

Fig. 2 CAD model of the triangular lip wall OWC

Table 1 Geometrical parameters

Orifice ratio (ϵ)	$\epsilon_1=0.4\%$	$\epsilon_2=0.58\%$	$\epsilon_3=0.79\%$	$\epsilon_4=1.03\%$	$\epsilon_5=1.3\%$
Relative opening (σ)	$\sigma_1=33\%$	$\sigma_2=50\%$	$\sigma_3=75\%$	-	-

Table 2 Mesh sizes

Sl. No.	Δx (m)	Δy (m)	Δz (m)	Nodes	Elements
Mesh 1	0.3736	0.3983	0.3991	128223	109760
Mesh 2	0.2982	0.3196	0.3237	227711	200580
Mesh 3	0.2483	0.2674	0.2701	388921	349668
Mesh 4	0.2475	0.2557	0.2656	422994	380748
Mesh 5	0.2133	0.2135	0.2166	686235	627200

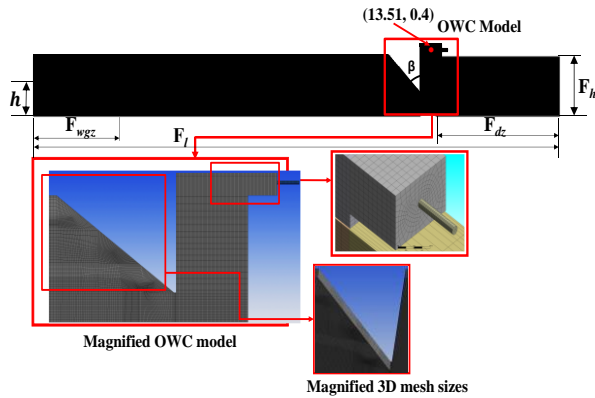


Fig. 3 Mesh structure near triangular lip wall

model parameters, ϵ , and σ , as indicated in Table 1, were used to analyze the performance of the OWC device.

Orifice ratio (ϵ): The orifice ratio, denoted by the symbol (ϵ), is calculated by dividing the cross-sectional area of the orifice ($A_0 = \frac{\pi}{4} c^2$) by the accessible free surface ($A_w = b \times w$) inside the chamber. Here, c is the orifice diameter. The ratio of these two areas is the orifice ratio.

Relative opening (σ): Relative opening is the ratio of the opening height of OWC (δ) to the water depth (h).

$$\epsilon = \frac{A_0}{A_w} \quad (20)$$

$$\sigma = \frac{\delta}{h} \quad (21)$$

An accurate representation of the fluid domain is executed via mesh refinement. Figure 3 shows an enlarged mesh size 3D OWC model to understand the numerical setup better. The rectangular grid sizes are discretized in the computational domain. During numerical investigation, 388,921 nodes are utilized in the Mesh 3 system (see Table 2), with domain divisions based on varying values of Δx , Δy , and Δz .

3.3 Grid Convergence Test

Pressure versus time (t) graphs are constructed to compare the mesh systems at different mesh numbers, as shown in Fig. 4. According to that, Mesh size parameters such as Mesh 1, 2, 3, 4, and 5 are shown in Table 2. It shows that mesh size decreased bit by bit. The five nodes correspond to 128233, 227711, 388921, 422994, and 686235. There is no variation in Mesh 3, Mesh 4, and Mesh 5, and consider the Mesh 3 system for numerical simulation. Here, the observation point is (13.51,0.4) at the middle point of the OWC device is considered for the grid convergence test. The system specifications are 64.0GB RAM and a 3.31GHz processor. Second-order upwind and first-order implicit schemes are used in the

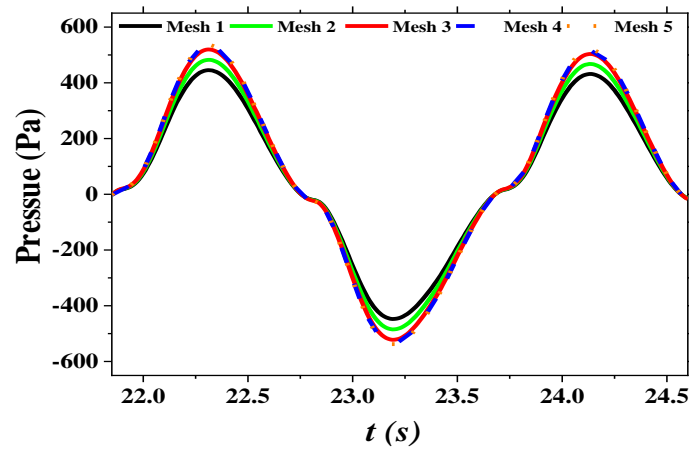


Fig. 4 Grid convergence at $H_i/\lambda = 0.02$, $T = 1.8s$, $\sigma = 75\%$, and $\varepsilon = 0.4\%$

Table 3 Wave parameters

Sl. no.	Wave Height (H_i)m	Wave Length (λ)m	Time Period (T)sec	Wave Steepness (H_i/λ)	Relative depth (h/λ)
1	0.07	3.8548	1.8	0.02	0.1556
2	0.08	2.7699	1.427	0.03	0.2166
3	0.09	2.2041	1.2365	0.04	0.2722
4	0.11	2.2738	1.26	0.045	0.2639
5	0.10	2.0019	1.168	0.05	0.2997

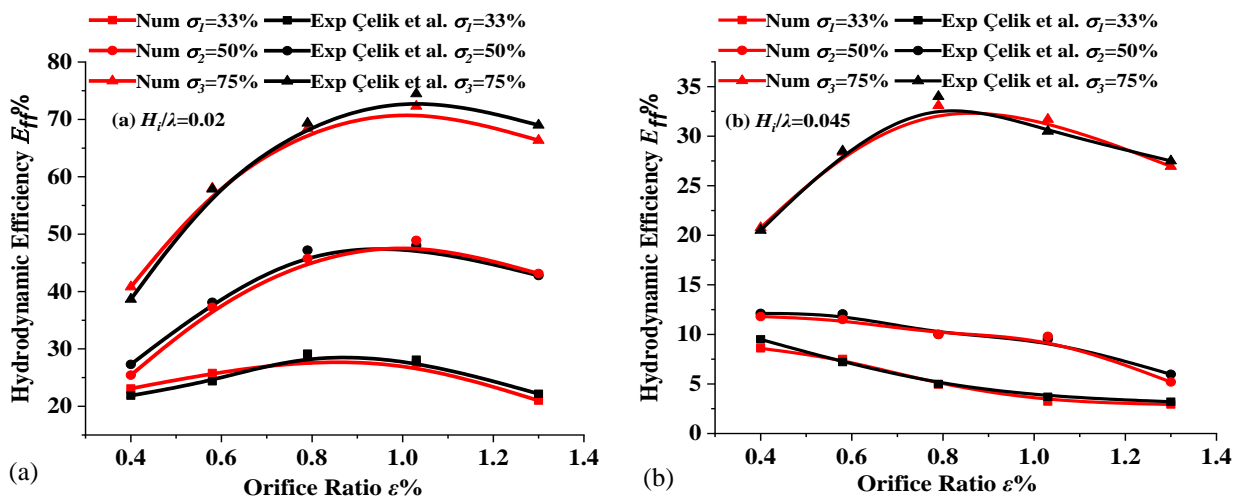


Fig. 5 Efficiency (E_{ff}) versus orifice ratio (ε): Validation between the present model and the published model (Çelik & Altunkaynak, 2019) at (a) $H_i/\lambda = 0.02$ and (b) $H_i/\lambda = 0.045$

discretization process. Choose time steps 0.01s and size of step time 2500. Iteration = 30 and Courant number = 0.25. It took a total of 26 hours to finish the simulation. Therefore, the present numerical model is approved and appropriate, and we can investigate further.

4. VALIDATION OF THE MODEL

The model was verified with the published experimental model done by Çelik and Altunkaynak (2019) and implemented for further improvement. The geometry of the numerical model is the same as that of the experimental model during validation. Wave parameters

are also the same. The depth of water at static conditions is 0.60 meters. The validation parameters are $H_i/\lambda = 0.02$ and 0.045 and $\sigma = 33\%$, 50%, and 75%, and wave parameters are shown in Table 3. Figure 5 illustrates that the proposed model is effectively accepted with the established investigative model. The fundamental geometry of each efficiency curve demonstrates adequate agreement for every value of relative opening (σ). Overall, there is good agreement between the experimental model and the proposed numerical model. For $H_i/\lambda = 0.02$, the maximal and minimal approximate errors were 3.88% and 0.14%, respectively. Similarly, at $H_i/\lambda = 0.045$, the maximal and minimal approximate errors were 2.10% and

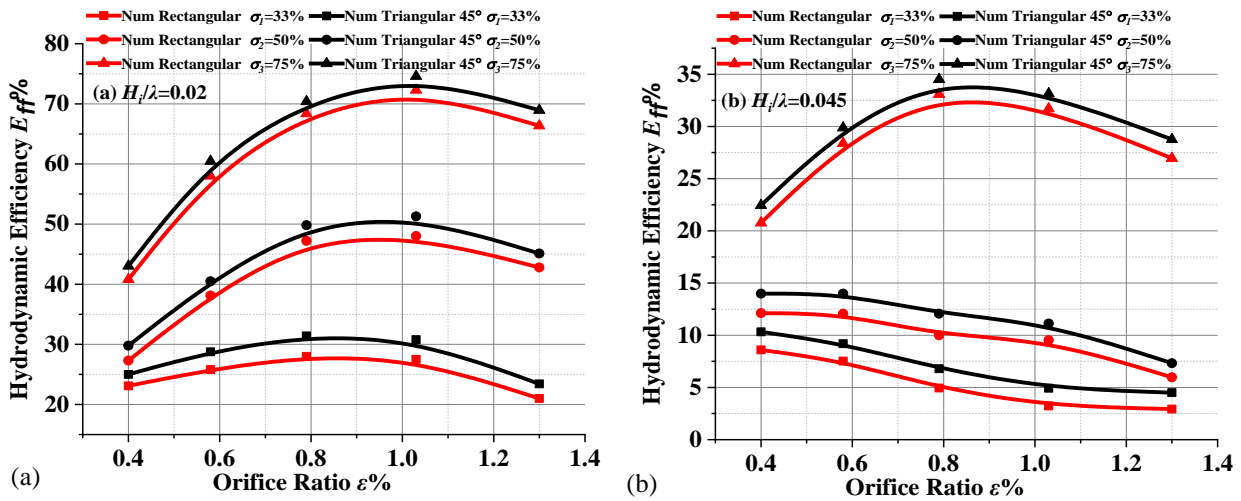


Fig. 6 Efficiency (E_{ff}) versus orifice ratio (ϵ): Comparison between the published numerical rectangular base model (Ranjan & DebRoy, 2023b) and the present numerical triangular model at (a) $H_i/\lambda = 0.02$ and (b) $H_i/\lambda = 0.045$

0.06%. Thus, the numerical model has been validated and appropriate and we can implement it to improve further. Such as the focus to be concentrated on the triangular lip wall OWC model. The graphs are shown in Figs. 6 (a&b) between hydrodynamic efficiency versus orifice ratio for a comparative discussion at $H_i/\lambda = 0.02$ and 0.045 between the published numerical rectangular base model (Ranjan & DebRoy 2023b) and the proposed triangular lip walls of an OWC device. In comparison with rectangular OWC, we have used 45° triangular lip walls by developing the geometrical layout of the OWC device. The figures show that the efficiency of the triangular lip walls OWC performs better than the rectangular OWC in each relative opening (σ) and orifice ratio (ϵ). Therefore, the proposed triangular lip walls numerical model is approved for further investigation to support the logic.

5. RESULTS AND DISCUSSION

5.1. Effect of Orifice Ratio

Two essential factors influence the turbine's damping. The first involves a large orifice diameter, while the second is a zero-orifice diameter. A very large orifice diameter means $A_o = A_w$, and according to Eq. (20), $\epsilon = 100\%$, and the zero-orifice diameter means $c = 0$, i.e., $A_o = 0$, and hence orifice ratio (ϵ) = 0%. The first case describes the air pressure $p(t)_{air}$ inside the chamber as zero. The second case, zero water velocity $v(t)$, is followed by Eq. (15). Therefore, for optimizing the orifice dimension, the product of water velocity and air pressure becomes maximal to extract the most significant wave energy from the incident wave.

Figures 7 to 11 show the graphs between hydrodynamic efficiencies versus orifice ratios at $\sigma = 33\%$, 50% , and 75% and $H_i/\lambda = 0.02, 0.03, 0.04, 0.045,$ and 0.05 . Graphs shapes are concave (Fig. 7), and the E_{ff} is maximum at $\sigma = 75\%$ for the OWC device. It has been observed that Fig. 7 indicates that at an orifice ratio ($\epsilon_1 = 0.4\%$), the power output remains low across all relative openings σ . This phenomenon is attributed to the damping

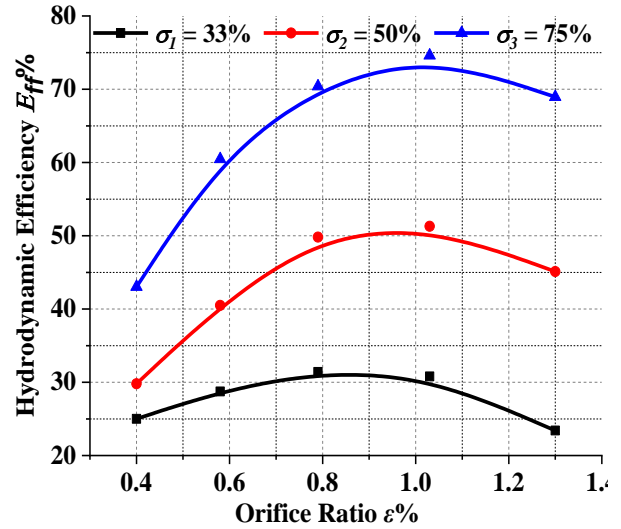


Fig. 7 Hydrodynamic efficiency v/s orifice ratio (ϵ) for $H_i/\lambda = 0.02$

effect caused by elevated air pressure within the OWC chamber, coupled with water's minimal free surface motion in the same chamber. When the ϵ increases, the efficiency initially rises to 1.03% and then drops off gradually. It has also been observed from Fig. 7 that at an orifice ratio ($\epsilon_4 = 1.03\%$), the power produced is maximum for all relative openings σ for the wave steepness $H_i/\lambda = 0.02$, and it becomes optimal. Further, at ($\epsilon_5 = 1.3\%$) orifice ratio, power production is also low for all relative openings σ owing to low air pressure and excessive water surface motion in the OWC chamber, causing damping. Figure 8 shows a relationship between hydrodynamic efficiency and orifice ratio at $H_i/\lambda = 0.03$. Observation shows that efficiency (E_{ff}) linearly decreases by the increasing orifice ratio (ϵ) at $\sigma_1 = 33\%$. Figure 8 shows that the graphs are concave at $\sigma_2 = 50\%$ and $\sigma_3 = 75\%$. For σ_2 and σ_3 , the efficiency reaches its peak at an orifice ratio of $\epsilon_2 = 0.58\%$ and $\epsilon_3 = 0.79\%$, respectively. Figure 9 illustrates the graphs at $H_i/\lambda = 0.04$. As the orifice ratio (ϵ)

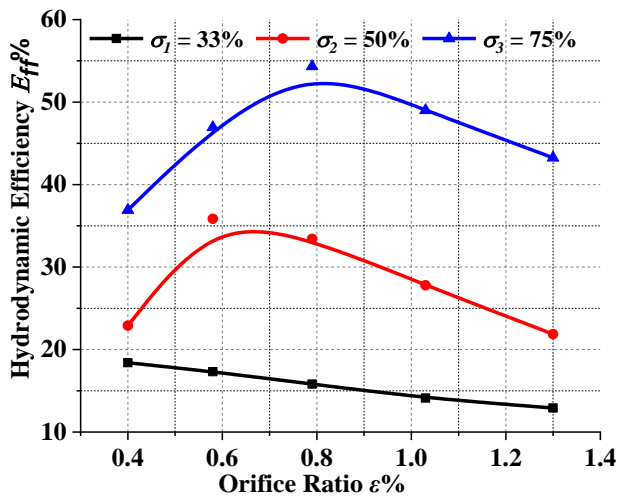


Fig. 8 Hydrodynamic efficiency v/s orifice ratio (ϵ) for $H_i/\lambda = 0.03$

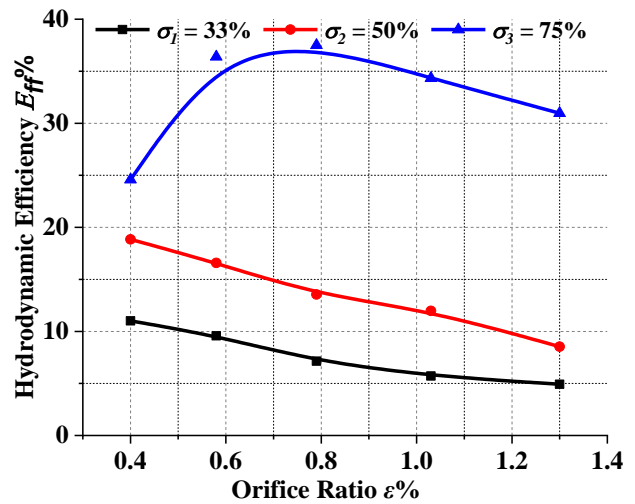


Fig. 9 Hydrodynamic efficiency v/s orifice ratio (ϵ) for $H_i/\lambda = 0.04$

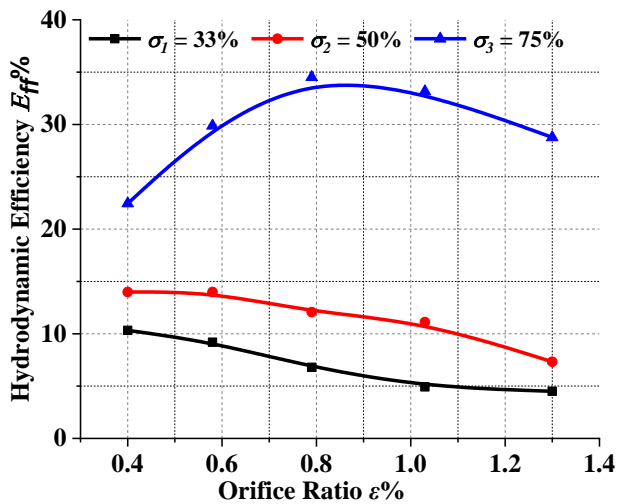


Fig. 10 Hydrodynamic efficiency v/s orifice ratio (ϵ) for $H_i/\lambda = 0.045$

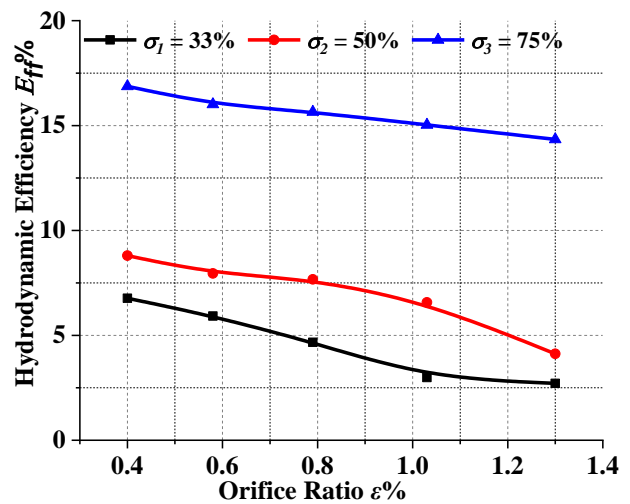


Fig. 11. Hydrodynamic efficiency v/s orifice ratio (ϵ) for $H_i/\lambda = 0.05$

increases, the hydrodynamic efficiency (E_{ff}) for relative openings $\sigma_1 = 33\%$ and $\sigma_2 = 50\%$ decreases linearly, whereas $\sigma_3 = 75\%$ results in a concave form.

The justification of hydrodynamic efficiency (E_{ff}) in Fig. 9-10 is the same, with the efficiency peaking at an orifice ratio of $\epsilon_3 = 0.79\%$ for σ_3 . At $\epsilon_1 = 0.40\%$, the wave energy converter performs at its peak for both σ_1 and σ_2 . The performance initially increases and then declines with the increases in orifice ratio (ϵ) for the relative opening $\sigma_3 = 75\%$. Maximum efficiency is achieved at σ_3 when the orifice ratio $\epsilon_3 = 0.79\%$. This analysis indicates that the OWC's performance follows a similar trend at $H_i/\lambda = 0.04$ and 0.45 . Figure 11 shows the peak performance at $\epsilon_1 = 0.40\%$ across all relative openings (σ), and the efficiency (E_{ff}) exhibits a linear decline as the orifice ratio (ϵ) increases. The preceding analysis of all Figs. 7 to 11 indicates that the efficiency (E_{ff}) is dependent upon H_i/λ . The efficiency (E_{ff}) gives the most favorable outcome at $H_i/\lambda = 0.02$ compared to others ($H_i/\lambda = 0.03, 0.04, 0.045,$ and 0.05), and the optimal performance of OWC is observed at $\epsilon_4 = 1.03\%$ and $\sigma_3 = 75\%$. The above

explanation shows that, at low incident waves and low wave steepness, the performance of the OWC is maximum. Finally, the outcome of the above explanation reveals that optimal damping not only depends on the wave steepness but also on the relative opening.

5.2 Effect of Pressure and Velocity

Figures 12(a-d) shows the dimensionless air pressure ($p/\rho g H_i$) and dimensionless vertical free surface velocity ($v/\sqrt{\lambda g}$) versus dimensionless time, t/T , in the same graphs. Higher air pressure is generated in the chamber at a low orifice ratio ($\epsilon_1 = 0.40\%$) compared to the other higher orifice ratios (such as $\epsilon_2 = 0.58\%$, $\epsilon_3 = 0.79\%$, and $\epsilon_4 = 1.03\%$). Therefore, the strengthened water column motion occurs at a lower orifice ratio. The high velocity of water surface motion and low air pressures occur in the chamber due to the oversized orifice. There is a dissimilar link between air pressure and the column's vertical water velocity. However, optimizing the orifice size requires extracting more output power from the OWC chamber. The observation from Fig. 12(d) shows the best result

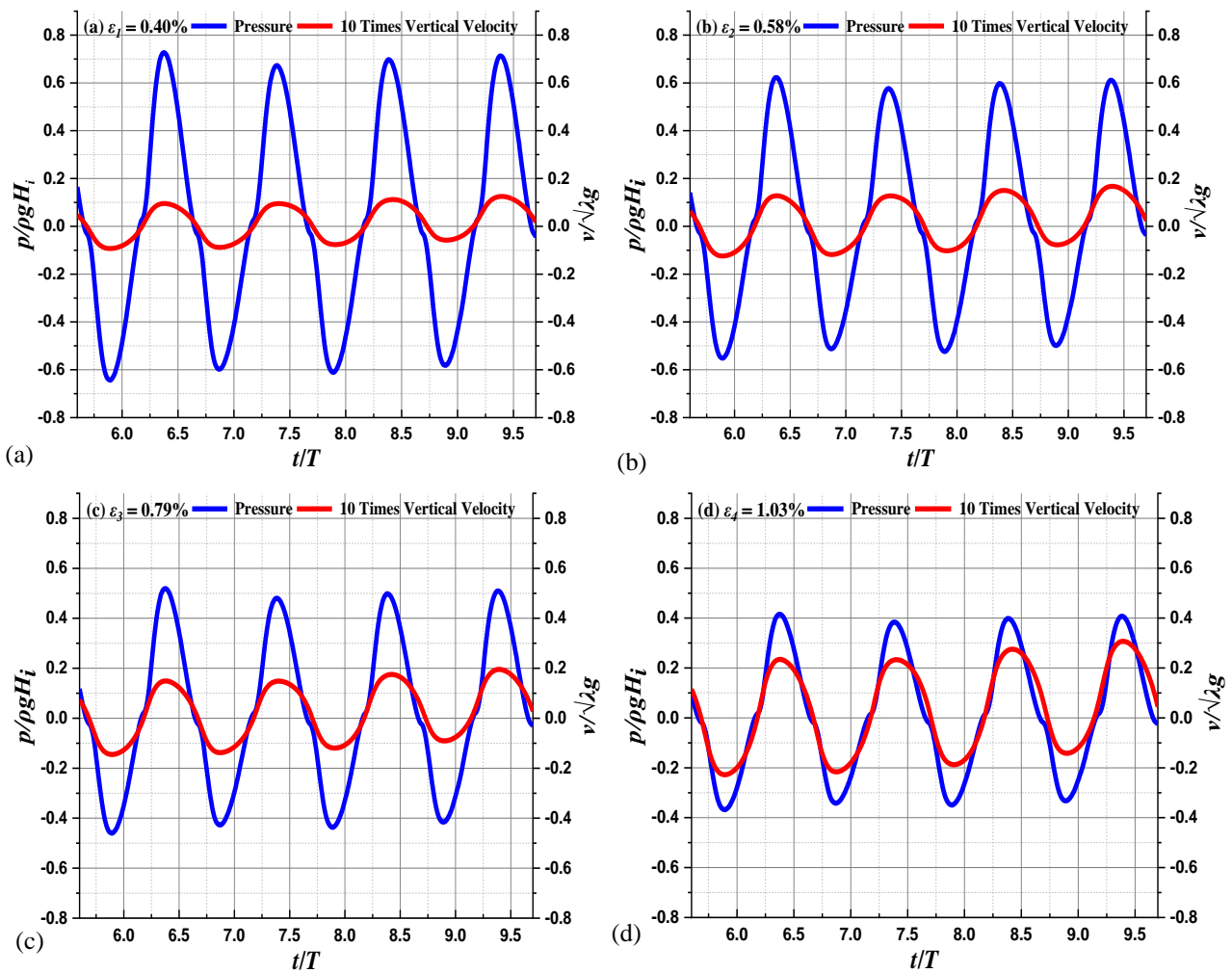


Fig. 12 (a-d) Non-dimensional air pressure and water surface velocity versus dimensionless time (t/T) in the OWC column at different orifice ratios (ϵ) and at $H_i/\lambda = 0.02$ and $\sigma_3 = 75\%$

obtained at an orifice ratio of 1.03% and wave steepness of 0.02 for a relative opening $\sigma_3 = 75\%$. The results for the other relative openings ($\sigma_1 = 33\%$ and $\sigma_2 = 50\%$) are the same that we have not summarised in this paper. It has to be noted by a closed observation that the positive top air pressure is more remarkable than the negative top air pressure. One possible explanation is that the air pressure within the chamber rises due to the water rising in the water column caused by the incident wave forces. The inhaling process begins to lower the chamber's air pressure as the water starts to return. Therefore, a non-linearity delay occurs between the exhalation and inhalation process. So, the exhalation of air in the chamber delays the air stay, which causes positive top air pressure rather than a negative top air pressure.

5.3. Outcome of Relative Opening

At various wave steepness (H_i/λ) and orifice ratios (ϵ), the relationship between efficiency (E_{ff}) and relative openings (σ) is shown in Figs. 13 to 17. It has been observed that efficiency increases with relative openings for all wave steepness conditions (H_i/λ). The efficiencies show more at $H_i/\lambda = 0.02$ than other wave steepness $H_i/\lambda = 0.03, 0.04, 0.045, 0.05$ for the same three relative openings. The performance of the OWC device is low at

the steepest incident wave $H_i/\lambda = 0.05$. The relative opening specification shows that the mouth opening is high for $\sigma_3 = 75\%$ and small for $\sigma_1 = 33\%$. Therefore, the finding suggests that larger relative openings allow the maximum amount of water due to incident waves in the chamber; hence, more energy becomes available for pneumatic energy conversion. For wave steepness 0.02 and 0.03, the performance increases linearly with relative openings.

In contrast, the efficiency increased exponentially for all wave steepness conditions. Figs 13 to 17 show that the efficiency reaches its highest value at a relative opening ($\sigma_3 = 75\%$). Figures 14-16 show the highest efficiency at $\sigma_3 = 75\%$ for ϵ_3 . Figure 17 shows that the efficiency of the OWC device is maximum at ϵ_1 for all relative openings (σ).

5.4. Effect of Wave Steepness

The curve shown in Fig. 18(a-c) illustrates the relationship between the efficiency (E_{ff}) of the energy converter and the steepness of the wave (H_i/λ) at various relative openings (σ) and orifice ratios (ϵ). The observation shows that wave steepness (H_i/λ) affects the efficiency (E_{ff}) of the converter. The efficiency linearly decreases by

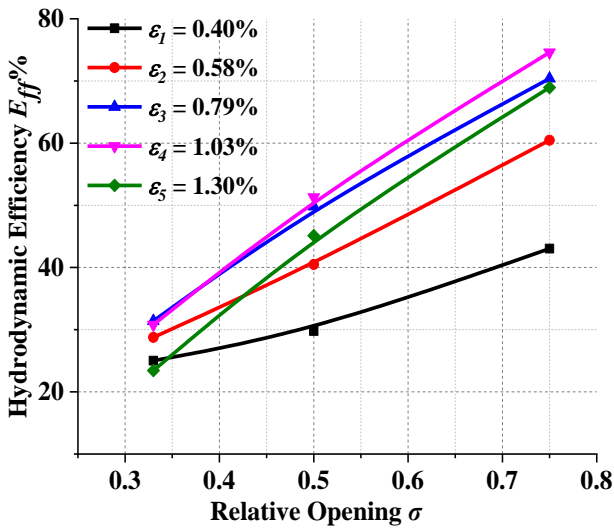


Fig. 13 Hydrodynamic efficiency v/s relative opening (σ) for $H_i/\lambda = 0.02$

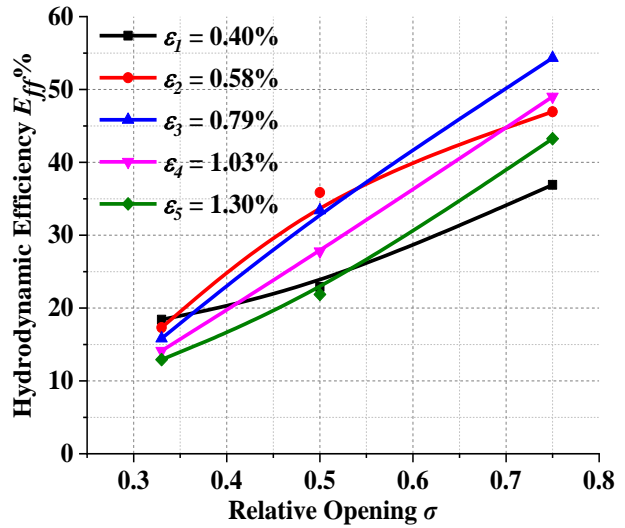


Fig. 14 Hydrodynamic efficiency v/s relative opening (σ) for $H_i/\lambda = 0.03$

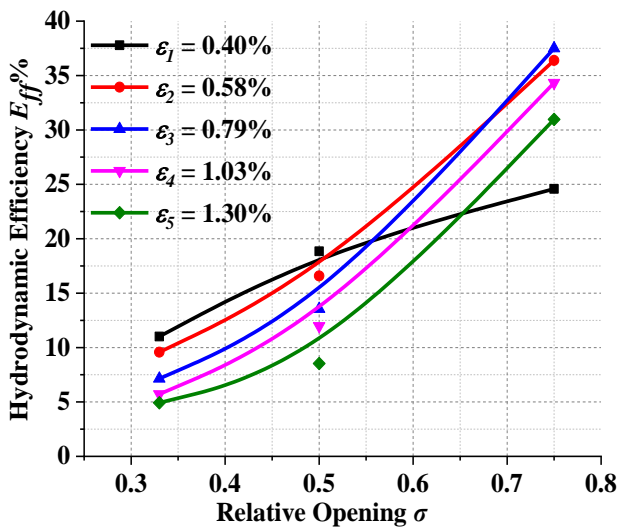


Fig. 15 Hydrodynamic efficiency v/s relative opening (σ) for $H_i/\lambda = 0.04$

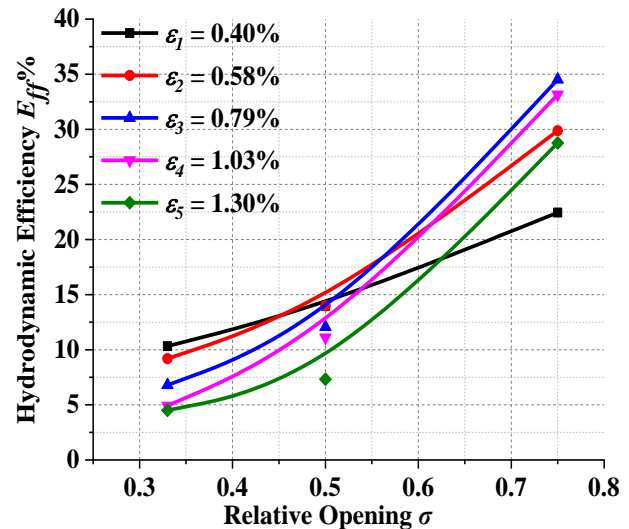


Fig. 16 Hydrodynamic efficiency v/s relative opening (σ) for $H_i/\lambda = 0.045$

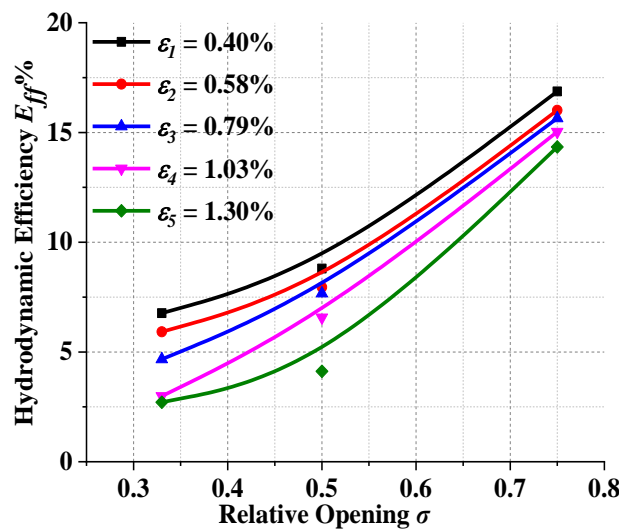
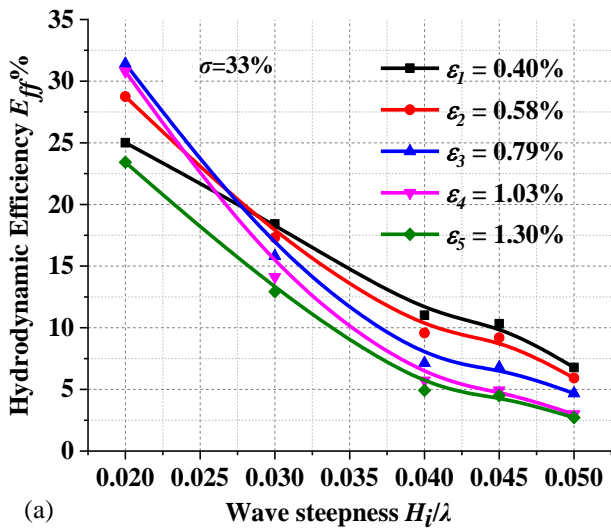
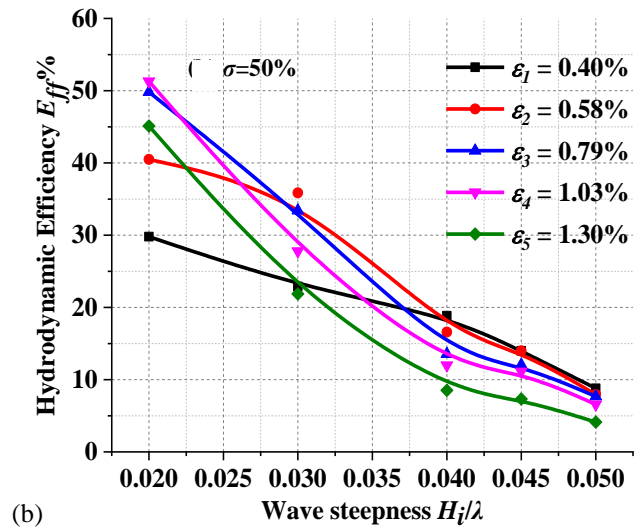


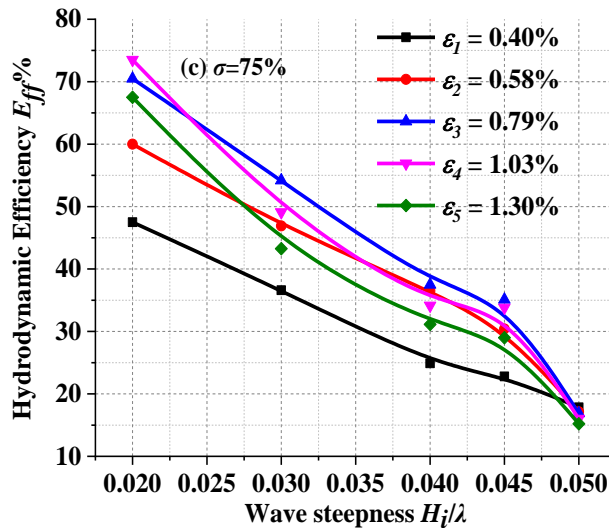
Fig. 17 Hydrodynamic efficiency v/s relative opening (σ) for $H_i/\lambda = 0.05$



(a) Fig. 18(a) Hydrodynamic efficiency v/s H_i/λ for different relative opening



(b) Fig. 18(b) Hydrodynamic efficiency v/s H_i/λ for different relative opening



(c) Fig. 18(c) Hydrodynamic efficiency v/s H_i/λ for different relative opening

increasing wave steepness, shown in Fig. 18, and the efficiency is prominent at $H_i/\lambda = 0.02$ for all values of σ . Figure 18(c) shows that the efficiency gradually converged at a value of $H_i/\lambda = 0.05$ and $\sigma = 75\%$.

5.5 Streamline Study

A streamlined study within the OWC chamber and the surrounding area near the lip wall is required to understand the effect of wave steepness on efficiency at $\sigma = 33\%$ and 75% . It has been studied that the exhalation and inhalation of air are complete for one wave cycle.

Figure 19 and 20 show the free surface and streamlined motion within the chamber at $\sigma = 33\%$ and 75% and $H_i/\lambda = 0.02$. It is shown in Fig. 19(a) that exhalation starts at $t/T = 9.83$ due to incident wave, and it is complete at time $t/T = 10.27$ (Fig. 19(c)). The free surface motion reaches its top level uniformly in the column shown in Fig. 19(b), which is maximum due to the exhalation of air pressure. Figure 19(a) shows vortex formation occurring near the lip wall and inside the chamber due to an incident wave that recommended that

water forcibly enter into the OWC chamber. After the exhalation, inhalation starts in Fig. 19(d) at $t/T = 10.33$, and it is complete at time $t/T = 10.77$ (Fig. 19(f)). The trend of motion of the free surface uniformly moves downwards due to the returning wave, which rushes out water from the chamber. The vortex formation occurs at $\sigma_l = 33\%$ in the chamber, indicating a minimal amount of flux entering into the chamber, causing the efficiency of OWC to reduce.

Figure 20 investigates the streamlined motion inside the chamber of the OWC wave energy converter for one wave at $H_i/\lambda = 0.02$, $\sigma_3 = 75\%$. The observation shows that the nature of exhalation and inhalation within the chamber is the same as the explanation done in Fig. 19. Figure 20(b) at time $t/T = 10.11$ maximum exhalation observed as no vortex formation within the chamber and stream line motion is smooth.

Therefore, a high flux volume enters into the chamber, causing the performance of the OWC to increase. The free surface reaches its top level uniformly in the column at that condition. Similarly, in Fig. 20(d),

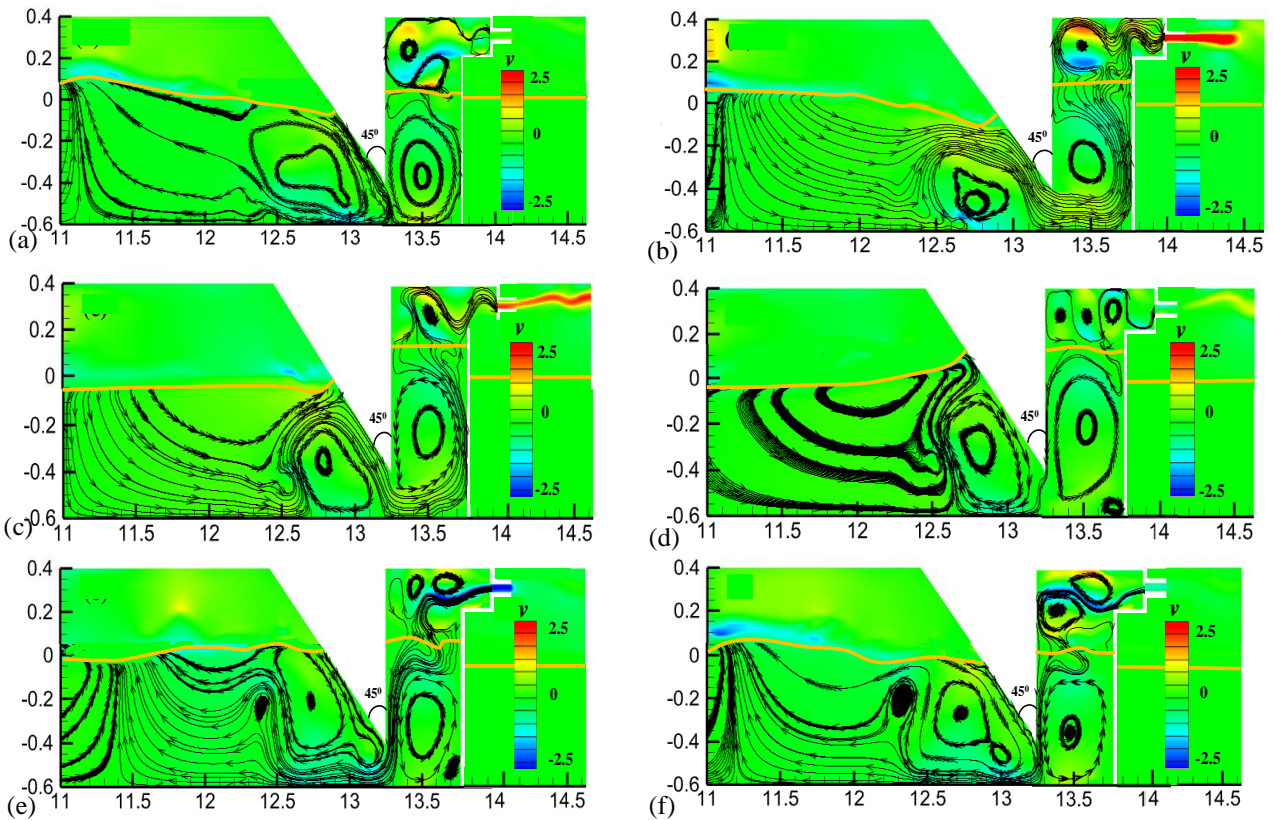


Fig. 19 Streamlines during exhalation and inhalation in the numerical simulation at $H_2/\lambda = 0.02$ and $\sigma_1 = 33\%$ based on one wave cycle. (a) $t/T=9.83$, (b) $t/T=10.05$, (c) $t/T=10.27$, (d) $t/T=10.33$, (e) $t/T=10.61$, (f) $t/T=10.77$

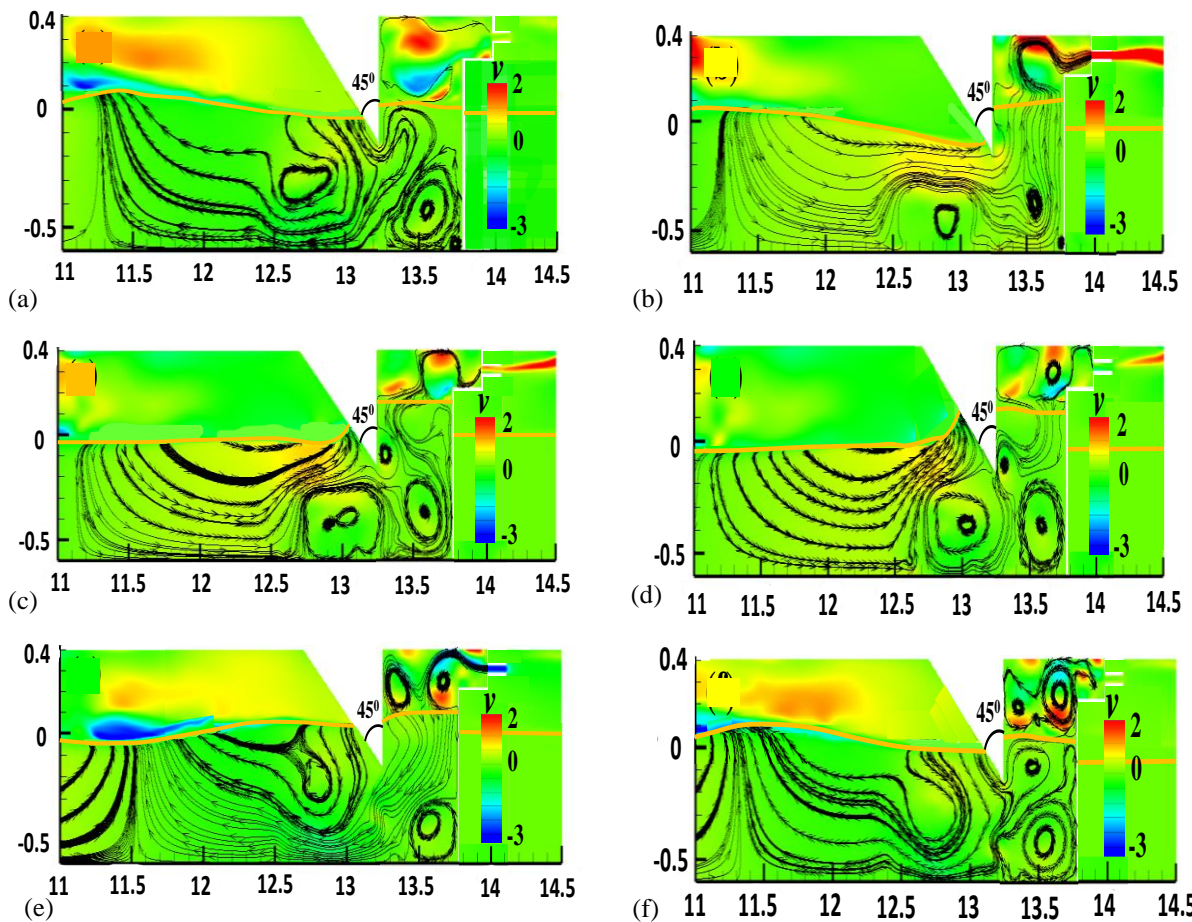


Fig. 20 Streamlines during exhalation and inhalation in the numerical simulation at $H_2/\lambda = 0.02$ and $\sigma_3 = 75\%$ based on one wave cycle. (a) $t/T=9.83$, (b) $t/T=10.11$, (c) $t/T=10.27$, (d) $t/T=10.33$, (e) $t/T=10.66$, (f) $t/T=10.83$

inhalation starts at time $t/T = 10.33$, and it is complete at time $t/T = 10.83$ (Fig. 20(f)). In this condition, the water surface is trying to rush out from the chamber due to the returning wave. Fig. 20(f) observation shows maximum inhalation. Based on the above explanation, it is clear that at $\sigma_3 = 75\%$, the flow of flux into the chamber is more dominant compared to a lesser opening $\sigma_1 = 33\%$ at $H_i/\lambda = 0.02$ and $\varepsilon_4 = 1.03\%$. Subsequently, the device absorbs more power.

6. CONCLUSION

Numerically investigated the performance of the triangular lip wall OWC model in a nonlinear wave field at different incident wave conditions, relative opening, and orifice ratio. This analysis uses commercial CFD code ANSYS FLUENT software in a 3D numerical wave tank. To achieve this task, the essential study in this model uses 45° triangular lip walls to improve the efficiency of the present OWC energy converter at three relative openings (σ_1 , σ_2 & σ_3) and five orifice ratios (ε_1 , ε_2 , ε_3 , ε_4 & ε_5) and five wave steepnesses (H_i/λ). The streamlined study within the OWC chamber and the surrounding area near the lip wall also require examination. The following points are the findings gained from the novel research.

1. The efficiency (E_{ff}) is affected by the steepness of the various incident wave (H_i/λ), relative opening (σ), and orifice ratios (ε).
2. The efficiency (E_{ff}) of the present model is not uniquely optimal. The optimal efficiency varies between the (ε) = 0.79% to 1.03% for all relative openings (σ) at $H_i/\lambda = 0.02$, and this value is 74.601% at $\varepsilon_4 = 1.03\%$, $\sigma_3 = 75\%$. Similarly, the optimal efficiency at $\varepsilon_3 = 0.79\%$, $\sigma_3 = 75\%$ and at $H_i/\lambda = 0.03$ is 54.33% and the efficiency at $H_i/\lambda = 0.04$ is 37.5% for $\varepsilon_3 = 0.79\%$, $\sigma_3 = 75\%$. The efficiency is 34.51% at $H_i/\lambda = 0.045$ for $\varepsilon_3 = 0.79\%$, $\sigma_3 = 75\%$. The efficiency is 16.87% at $H_i/\lambda = 0.05$ for $\varepsilon_1 = 0.40\%$, $\sigma_3 = 75\%$. Therefore, optimal efficiency is a function of incident wave characteristics, the chamber's relative opening, and the orifice ratio.
3. The efficiency (E_{ff}) improved with the relative opening (σ) at each wave steepness (H_i/λ). The highest efficiency occurs at $H_i/\lambda = 0.02$, $\sigma_3 = 75\%$, and $\varepsilon_4 = 1.03\%$ due to low wave reflection from the front wall.
4. The E_{ff} decreases by the rise of H_i/λ and is the inverse relationship between E_{ff} & H_i/λ . At low wave steepness, efficiency is greater & at high wave steepness; efficiency is low. 74.601% is the maximal efficiency achieved at $\varepsilon_4 = 1.03\%$, $\sigma_3 = 75\%$, $H_i/\lambda = 0.02$, and the efficiency gradually convergence occurred at a value of $H_i/\lambda = 0.05$ and $\sigma_3 = 75\%$.
5. The results of the hydrodynamic performance are affected by the streamlined study. The device absorbs more power when a high flux volume enters the chamber at a relative openness $\sigma_3 = 75\%$ instead of a low volume at $\sigma_1 = 33\%$.
6. Workable energy is obtained by choosing wave parameters, relative opening height, and orifice ratio.

ACKNOWLEDGEMENTS

I am grateful to the Department of Mechanical Engineering at NIT Silchar, Assam, for their assistance in developing the simulation laboratory.

CONFLICT OF INTEREST

The authors have no conflicts to disclose.

AUTHORS CONTRIBUTION

Pradip Deb Roy developed the ideas; formulation or evolution of research goals and aims and analyzed the study data. Deb Roy also develop of methodology and creation of models. **Ravi Ranjan Manjul** numerically solved the problem using Ansys Fluent software and drew all the graphs and validation and comparison. Both authors discussed the results and contributed to the final manuscript. Finally, Deb Roy drafted and edited the manuscript and took oversight and leadership responsibility for the research activity planning and execution.

REFERENCES

- Ashlin, S. J., Sundar, V., & Sannasiraj, S. A. (2016). Effects of bottom profile of an oscillating water column device on its hydrodynamic characteristics. *Renewable Energy*, 96, 341-353. <https://doi.org/10.1016/j.renene.2016.04.091>
- Bouali, B., & Larbi, S. (2013). Contribution to the geometry optimisation of an oscillating water column wave energy converter. *Energy Procedia*, 36, 565-573. <https://doi.org/10.1016/j.egypro.2013.07.065>
- Brito, M., Ferreira, R. M. L., Teixeira, L., Neves, M. G., & Gil, L. (2020). Experimental investigation of the flow field in the vicinity of an oscillating wave surge converter. *Journal of Marine Science and Engineering* 8(976), 1-18. <https://doi.org/10.3390/jmse8120976>
- Carlo, L., Iuppa, L., & Faraci, C. (2023). A numerical-experimental study on the hydrodynamic performance of a U-OWC wave energy converter. *Renewable Energy*, 203, 89-101. <https://doi.org/10.1016/j.renene.2022.12.057>
- Çelik, A., & Altunkaynak, A. (2018). Experimental and analytical investigation on chamber water surface fluctuations and motion behaviours of water column type wave energy converter. *Ocean Engineering*, 150, 209-220. <https://doi.org/10.1016/j.oceaneng.2017.12.065>
- Çelik, A., & Altunkaynak, A. (2019). Experimental investigations on the performance of a fixed-oscillating water column type wave energy converter. *Energy*, 188, 116071. <https://doi.org/10.1016/j.energy.2019.116071>
- Çelik, A., & Altunkaynak, A. (2020). Estimation of water column surface displacement of a fixed oscillating

- water column by simple mechanical model with determination of hydrodynamic parameters via physical experimental model. *Journal of Waterway, Port, Coastal, and Ocean Engineering*, 146(5), 04020030.
[http://dx.doi.org/10.1061/\(ASCE\)WW.1943-5460.0000593](http://dx.doi.org/10.1061/(ASCE)WW.1943-5460.0000593)
- Çelik, A., & Altunkaynak, A. (2021). An in depth experimental investigation into effects of incident wave characteristics front wall opening and PTO damping on the water column displacement and air differential pressure in an OWC chamber. *Energy*, 230, 120827.
<https://doi.org/10.1016/j.energy.2021.120827>
- Çelik, A., (2022). An experimental investigation into the effects of front wall geometry on OWC performance for various levels of applied power take-off dampings. *Ocean Engineering*, 248, 110761.
<https://doi.org/10.1016/j.oceaneng.2022.110761>
- Cruz-Pérez, N., Alcántara, J. S. R., Koronaiou, V. L. P., Jančula, A., Martín, J. R., García-Gil, A., Fontes, J. C., & Santamarta, J. C. (2024). SWOT analysis of the benefits of hydropower energy in four archipelagos. *Civil Engineering Journal* (E-ISSN: 2476-3055; ISSN: 2676-6957), 10(07), 2370-2383.
<http://dx.doi.org/10.28991/CEJ-2024-010-07-019>
- Dizadji, N., & Sajadian, S. E. (2011). Modeling and optimization of the chamber of OWC system. *Energy*, 36(5), 2360-2366.
<https://doi.org/10.1016/j.energy.2011.01.010>
- Falcão, A. F., & Henriques, J. C. (2016). Oscillating-water-column wave energy converters and air turbines: A review. *Renewable Energy*, 85, 1391-1424. <https://doi.org/10.1016/j.renene.2015.07.086>
- Gonçalves, R. A. A. C., Teixeira, P. R. F., Didier, E., & Torres, F. R. (2020). Numerical analysis of the influence of air compressibility effects on an oscillating water column wave energy converter chamber. *Renewable Energy*, 153, 1183-1193.
<https://doi.org/10.1016/j.renene.2020.02.080>
- Gouaud, F., Rey, V., Piazzola, J., & Van Hooff, R. (2010). Experimental study of the hydrodynamic performance of an onshore wave power device in the presence of an underwater mound. *Coastal Engineering*, 57(11-12), 996-1005.
<https://doi.org/10.1016/j.coastaleng.2010.06.003>
- Hirt, C. W., & Nichols, B. D. (1981). Volume of fluid (VOF) method for the dynamics of free boundaries. *Journal of Computational Physics*, 39(1), 201-225.
[https://doi.org/10.1016/0021-9991\(81\)90145-5](https://doi.org/10.1016/0021-9991(81)90145-5)
- Hotta, H., Miyazaki, T., Washio, Y., & Ishii, S. (1988). *On the performance of the wave power device Kaimei—the results on the open sea tests*. Proceedings of the Seventh International Conference on Offshore Mechanics and Arctic Engineering, Houston, TX, USA.
- Iturrioz, A., Guanche, R., Lara, J. L., Vidal, C., & Losada, I. J. (2015). Validation of OpenFOAM® for oscillating water column three-dimensional modeling. *Ocean Engineering*, 107, 222-236.
<https://doi.org/10.1016/j.oceaneng.2015.07.051>
- Launder, B. E. (1989). Second-moment closure and its use in modelling turbulent industrial flows. *International Journal for Numerical Methods in Fluids*, 9, 963-985.
<https://doi.org/10.1002/flid.1650090806>
- Liu, Z., Hyun, B., Jin, J., Hong, K., & Lee, Y. (2016). OWC air chamber performance prediction under impulse turbine damping effects. *Science China Technological Sciences*, 59, 657-666.
<https://doi.org/10.1007/s11431-016-6030-5>
- López, I., Pereiras, B., Castro, F., & Iglesias, G. (2014). Optimisation of turbine-induced damping for an OWC wave energy converter using a RANS-VOF numerical model. *Applied Energy*, 127, 105-114.
<https://doi.org/10.1016/j.apenergy.2014.04.020>
- Malmö, O., & Reitan, A. (1985). Wave-power absorption by an oscillating water column in a channel. *Journal of Fluid Mechanics*, 158, 153-175.
<https://doi.org/10.1017/S0022112085002592>
- Malmö, O., & Reitan, A. (1986). Wave-power absorption by an oscillating water column in a reflecting wall. *Applied Ocean Research*, (United Kingdom), 8(1).
[https://doi.org/10.1016/S0141-1187\(86\)80030-X](https://doi.org/10.1016/S0141-1187(86)80030-X)
- Marjani, A. El., Castro, F., Rodriguez, M. A., & Santos, M. T. P. (2008). Numerical modelling in wave energy conversion systems. *Energy*, 33, 1246-1253.
<https://doi.org/10.1016/j.energy.2008.02.018>
- Morris-Thomas, M. T., Irvin, R. J., & Thiagarajan, K. P. (2007). An investigation into the hydrodynamic efficiency of an oscillating water column. *J, V, PP*.
<https://doi.org/10.1115/1.2426992>
- Ning, D. Z., Shi, J., Zou, Q. P., & Teng, B. (2015). Investigation of hydrodynamic performance of an OWC (oscillating water column) wave energy device using a fully nonlinear HOBEM (higher-order boundary element method). *Energy*, 83, 177-188.
<https://doi.org/10.1016/j.energy.2015.02.012>
- Ning, D. Z., Wang, R. Q., Zou, Q. P., & Teng, B. (2016). An experimental investigation of hydrodynamics of a fixed OWC Wave Energy Converter. *Applied Energy*, 168, 636-648.
<https://doi.org/10.1016/j.apenergy.2016.01.107>
- Pinson, P., Reikard, G., & Bidlot, J. R. (2012). Probabilistic forecasting of the wave energy flux. *Applied Energy*, 93, 364-370.
<https://doi.org/10.1016/j.apenergy.2011.12.040>
- Pontes, M. T., & Falcao, A. N. T. Ó. N. I. O. (2001, October). *Ocean energies: resources and utilisation*. world energy council. 18th Congress, Buenos Aires.
- Ranjan, S., & DebRoy, P. (2023a). Numerically investigated the performance of parabolic bottom profile land-fixed OWC by changing the orifice ratio and relative opening. *Arabian Journal for Science and Engineering* 48, 12091–12105.
<https://doi.org/10.1007/s13369-023-07677-0>

- Ranjan, S., & DebRoy, P. (2023b). Numerical investigation of optimal hydrodynamic performance by changing the orifice ratio and relative opening of a land-fixed rectangular-based OWC. *Journal of Applied Fluid Mechanics*, *16*(11), 2263-2276. <https://doi.org/10.47176/jafm.16.11.1799>
- Rodríguez, A. A. M., Vanegas, G. P., Serratos, B. E. V., Martínez, I. O., Mendoza, E., Ilzarbe, J. M. B., Sundar, V., & Silva, R. (2023). The hydrodynamic performance of a shore-based oscillating water column device under random wave conditions. *Ocean Engineering*, *269*, 113573. <https://doi.org/10.1016/j.oceaneng.2022.113573>
- Rusvan, A. A., Maricar, F., Thaha, M. A., & Paotonan, C., (2024) Evaluation of tidal energy potential using a two-way tidal energy model. *Civil Engineering Journal*, *10*, (09), 3011-3033. <http://dx.doi.org/10.28991/CEJ-2024-010-09-016>
- Simonetti, I., & Cappiotti, L., (2021) Hydraulic performance of oscillating water column structures as anti-reflection devices to reduce harbour agitation. *Coastal Engineering* *165*, 103837. <https://doi.org/10.1016/j.coastaleng.2020.103837>
- Simonetti, I., Cappiotti, L., Elsafti, H., & Oumeraci, H. (2017). Optimization of the geometry and the turbine induced damping for fixed detached and asymmetric OWC devices: A numerical study. *Energy*, *139*, 1197-1209. <https://doi.org/10.1016/j.energy.2017.08.033>
- Sukkee, M., & Kongphan, P., (2024). Innovative Metal Powder Production Using CFD with Convergent-Divergent Nozzles in Wire Arc Atomization. *HighTech and Innovation Journal*, *5*(3), 551-571. <http://dx.doi.org/10.28991/HIJ-2024-05-03-02>
- Teixeira, P. R. F., Davyt, D. P., Didier, E., & Ramalhais, R., (2013). Numerical simulation of an oscillating water column device using a code based on Navier-Stokes equations. *Energy*, *61*, 513-530. <https://doi.org/10.1016/j.energy.2013.08.062>
- Thiruvenkatasamy, K., & Neelamani, S. (1997). On the efficiency of wave energy caissons in array. *Applied Ocean Research*, *19*(1), 61-72. [https://doi.org/10.1016/S0141-1187\(97\)00008-4](https://doi.org/10.1016/S0141-1187(97)00008-4)
- Tseng, R. S., Wu, R. H., & Huang, C. C. (2000). Model study of a shoreline wave-power system. *Ocean Engineering*, *27*(8), 801-821. [https://doi.org/10.1016/S0029-8018\(99\)00028-1](https://doi.org/10.1016/S0029-8018(99)00028-1)
- Vicinanza, D., Contestabile, P., Nørgaard, J. Q. H., & Andersen, T. L., (2014) Innovative rubble mound breakwaters for overtopping wave energy conversion, *Coastal Engineering* *88*, 154-170. <http://dx.doi.org/10.1016/j.coastaleng.2014.02.004>
- Vicinanza, D., Lauro, E. D., Contestabile, P., Gissonni, C., Lara, J. L., & Losada, I. J., (2019). Review of innovative harbor breakwaters for wave-energy conversion, *Journal of Waterway, Port, Coastal, and Ocean Engineering* *145* (4), 03119001-18. [http://dx.doi.org/10.1061/\(ASCE\)WW.1943-5460.0000519](http://dx.doi.org/10.1061/(ASCE)WW.1943-5460.0000519)
- Washio, Y., Osawa, H., Nagata, Y., Furuyama, H., & Fujita, T. (2000). *The offshore floating type wave power device 'Mighty Whale': open sea tests*. Proceedings of the 10 International Offshore and Polar Engineering Conference, 373-380, Seattle, USA. <https://onepetro.org/ISOPEIOPEC/proceedings-abstract/ISOPE00/All-ISOPE00/6815>
- Whittaker, T. J. T., McIlwaine, S. J., & Raghunathan, S. (1993, July). *A review of the Islay shoreline wave power station*. Proceedings of First European Wave Energy Symposium.
- Yadav, S. S., & DebRoy, P. (2022). Generation of stable linear waves in shallow water in a Numerical wave tank. *Journal of Applied Fluid Mechanics*, *15*(2), 537-549. <https://doi.org/10.47176/jafm.15.02.32987>